Tidal dispersion in short estuaries

Adrian Mikhail Palaci Garcia[1] and W Rockwell Geyer[2]

[1]MIT-WHOI Joint Program in Applied Ocean Science & Engineering
[2]Woods Hole Oceanographic Institution

November 26, 2022

Abstract

The salinity distribution of an estuary depends on the balance between the river outflow, which is seaward, and a dispersive salt flux, which is landward. The dispersive salt flux at a fixed cross-section can be divided into shear dispersion, which is caused by spatial correlations of the cross-sectionally varying velocity and salinity, and the tidal oscillatory salt flux, which results from the tidal correlation between the cross-section averaged, tidally varying components of velocity and salinity. The theoretical moving plane analysis of Dronkers and van de Kreeke (1986) indicates that the oscillatory salt flux is exactly equal to the difference between the "local" shear dispersion at a fixed location and the shear dispersion which occurred elsewhere within a tidal excursion – therefore, they refer to the oscillatory salt flux as "nonlocal" dispersion. We apply their moving plane analysis to a numerical model of a short, tidally dominated estuary and provide the first quantitative confirmation of the theoretical result that the spatiotemporal variability of shear dispersion accounts for the oscillatory salt flux. Shear dispersion is localized in space and time due to the tidal variation of currents and the position of the along-channel salinity distribution with respect to topographic features. We find that dispersion near the mouth contributes strongly to the salt balance, especially under strong river and tidal forcing. Additionally, while vertical shear dispersion produces the majority of dispersive salt flux during neap tide and high flow, lateral mechanisms provide the dominant mode of dispersion during spring tide and low flow.

Tidal dispersion in short estuaries

Adrian Mikhail P. Garcia[1,2,*], W. Rockwell Geyer[2]

[1]MIT-WHOI Joint Program in Applied Ocean Science & Engineering, Cambridge, MA, USA

[2]Woods Hole Oceanographic Institution, Woods Hole, MA, USA

[*]Corresponding author: Adrian Mikhail P. Garcia (garciaap@mit.edu)

Key Points:

- Application of a tidally moving plane framework demonstrates that all landward salt flux results from shear dispersion
- Shear dispersion is spatiotemporally variable in estuaries and is most pronounced near topographic features, such as the mouth
- The primary mode of dispersion transitions from lateral to vertical shear dominant as river flow increases and tidal currents weaken

Abstract

The salinity distribution of an estuary depends on the balance between the river outflow, which is seaward, and a dispersive salt flux, which is landward. The dispersive salt flux at a fixed cross-section can be divided into shear dispersion, which is caused by spatial correlations of the cross-sectionally varying velocity and salinity, and the tidal oscillatory salt flux, which results from the tidal correlation between the cross-section averaged, tidally varying components of velocity and salinity. The theoretical moving plane analysis of Dronkers and van de Kreeke (1986) indicates that the oscillatory salt flux is exactly equal to the difference between the "local" shear dispersion at a fixed location and the shear dispersion which occurred elsewhere within a tidal excursion – therefore, they refer to the oscillatory salt flux as "nonlocal" dispersion. We apply their moving plane analysis to a numerical model of a short, tidally dominated estuary and provide the first quantitative confirmation of the theoretical result that the spatiotemporal variability of shear dispersion accounts for the oscillatory salt flux. Shear dispersion is localized in space and time due to the tidal variation of currents and the position of the along-channel salinity distribution with respect to topographic features. We find that dispersion near the mouth contributes strongly to the salt balance, especially under strong river and tidal forcing. Additionally, while vertical shear dispersion produces the majority of dispersive salt flux during neap tide and high flow, lateral mechanisms provide the dominant mode of dispersion during spring tide and low flow.

Plain Language Summary

The length of salinity intrusion in an estuary depends on the balance between the river outflow, which is directed seaward, and a dispersive salt flux, which is directed landward. The dispersive salt flux at a fixed location can be divided into shear dispersion – the spatial correlation of velocity and salinity over a cross-section – and the tidal oscillatory salt flux – the temporal correlation of velocity and salinity over a tidal cycle. By analyzing salt fluxes in a plane that moves back and forth with the tide, we show how all dispersive salt flux ultimately results from shear dispersion within the estuary and adjacent coastal waters. Shear dispersion varies significantly in space and time and is most pronounced near topographic features such as constrictions and the estuary mouth. By utilizing a moving plane framework, we show that dispersion near the mouth contributes significantly to the salt balance of the estuary, especially under high river flow conditions when the estuary length becomes short. Furthermore, we find that the primary mode of dispersion varies from lateral to vertical shear as river flow increases or tidal currents weaken.

1 Introduction

The salt balance in an estuary depends on the river flow, which exports salt from the estuary, and the total sum of dispersive mechanisms, which act to transport salt into the estuary. In long estuaries where the lengthscale of the salinity intrusion is much greater than the tidal excursion, the salt balance is maintained primarily by the estuarine circulation due to gravitational circulation (Chatwin, 1976; Chen et al., 2012; Hansen & Rattray, 1965) and tidal straining (Burchard & Hetland, 2010; Simpson et al., 1990). However, in short estuaries where the lengthscale of the salinity intrusion is similar to the tidal excursion length, dispersion by tidal processes becomes the dominant mode of landward salt flux (Chen et al., 2012).

Tidal dispersion results from oscillatory boundary layer shear as well as interactions between the tidal currents and the local bathymetry, resulting in tidal variations of the salinity field that produce a net dispersive salt flux (Fischer et al., 1979; Geyer & Signell, 1992; Zimmerman, 1986). Mechanisms of tidal dispersion include oscillatory shear dispersion (Bowden, 1965), jet-sink exchange at constrictions (Chen et al., 2012; Fram et al., 2007; Stommel & Farmer, 1952), and tidal trapping in shallow lateral zones such as shoals and mudflats (Dronkers, 1978; Okubo, 1973; Ralston & Stacey, 2005). Notably, each of these processes represents spatial variations of velocity and salinity over cross-sectional planes and are thus manifestations of the shear dispersion mechanism as first described by Taylor (1953, 1954).

Even in the absence of shear dispersion, i.e., where there are no spatial correlations of salinity and velocity, tidal dispersion may occur due to the correlation of the tidally varying, cross-sectionally averaged velocity and salinity. The importance of this tidal oscillatory salt flux term, sometimes called tidal pumping (Fram et al., 2007; West et al., 1990), has been observed in partially mixed estuaries such as the Hudson (Hunkins, 1981; Lerczak et al., 2006), Tamar (Uncles

et al., 1985), Volkerak (Dronkers & van de Kreeke, 1986), and Conwy (Simpson et al., 2001) rivers, and in salt wedge estuaries such as the Columbia (Hughes & Rattray, 1980) and Merrimack (Chen et al., 2012) rivers. However, the mechanisms that produce this tidal salt flux term are usually left unexplained.

Dronkers and van de Kreeke (1986) provided key insight into this tidal oscillatory salt flux. They adopted a "moving plane" coordinate system to demonstrate that the tidally averaged salt flux through a fixed cross-section is equal to the tidally averaged salt flux through a plane moving with the tides if they have the same tidally averaged salinity. In the moving plane, all dispersive salt results only from shear dispersion. This is because within that quasi-Lagrangian coordinate system, the tidally varying cross-sectionally averaged velocity is always zero and therefore the dispersive salt flux can only be produced by the correlation of velocity and salinity deviations from their cross-sectional averages. By equating the transport in the fixed and moving reference frames, they demonstrated that the tidal oscillatory salt flux represents the difference between the shear dispersion that occurs elsewhere within a tidal excursion of the fixed location and the "local" shear dispersion at that fixed location. Therefore, they called the tidal oscillatory salt flux the "nonlocal" salt flux. While they provided the theoretical framework for understanding nonlocal dispersion, they did not provide a quantitative analysis of the local sources of nonlocal dispersion for the case study they examined. Furthermore, the quantitative application of the Dronkers and van de Kreeke (1986) moving plane theory has not been attempted in subsequent studies.

The key objective of this study is to quantify how dispersive mechanisms associated with topographic features directly contribute to the maintenance of the salinity distribution in numerical simulations of a short, shallow estuary by applying the methodology of Dronkers and van de Kreeke (1986), henceforth referred to as DvdK86. Section 2 describes the model setup used for

the analysis. Then, in section 3, we describe the salt flux decomposition using both the Eulerian framework as well as the DvdK86 moving plane approach. In section 4, we present the results of the salt flux decomposition and then highlight various regions and times exhibiting locally high shear dispersion, as these are the primary sources of the dispersive salt flux. Additionally, we vary forcing conditions and examine their impact on the estuarine salinity structure and transport processes. In section 5, we discuss the dominant mechanisms of dispersion and the salt balance in short, tidally dominated estuaries. Finally, we provide a summary of our results and give conclusions in section 6.

2 Model

Our idealized numerical model is based on the North River, (Marshfield, MA) a short, salt-marsh estuary which ranges from well-mixed to stratified depending on forcing conditions. In the North River, the salinity intrusion length varies from about 7–20 km while the tidal excursion length ranges from about 4–9 km. Previous field studies have determined that nonlocal dispersion plays a dominant role in the landward salt flux at a mooring located about 4 km from the mouth (Garcia et al., 2021). Thus, one of the motivations of this study was to identify the mechanisms responsible for producing the nonlocal salt flux in estuaries similar to the North River where tidal dispersive processes may be particularly important.

We built an idealized model of an estuary-shelf system (see Figure 1) using the Regional Ocean Modeling System (ROMS), a 3-D, hydrostatic, Boussinesq, primitive equation model with terrain-following, vertically-stretched coordinates on a structured grid (Haidvogel et al., 2008; Shchepetkin & McWilliams, 2005). The grid is rectilinear in the coastal ocean, which extends 10 km in the cross-shore direction and 5 km in the along-shore direction, with high resolution of 50 m near the estuarine channel, telescoping 250 m in the far field. The depth across the shelf varies

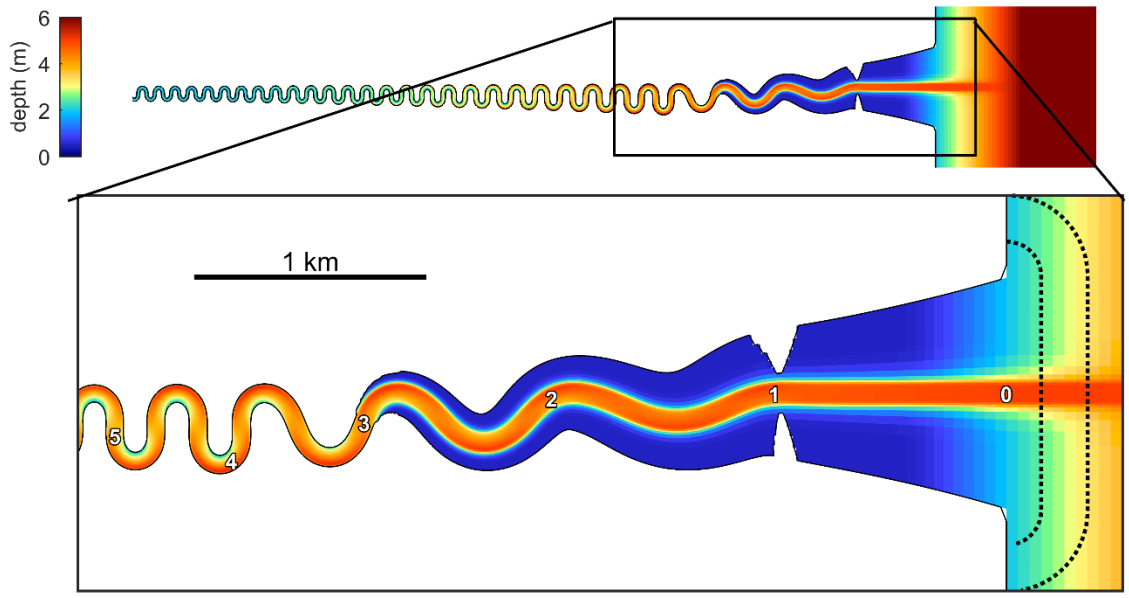

Figure 1. Model domain in the main region of the estuary-shelf system. A constriction is located at 1 km and the shoals converge at 3 km from the mouth. Along-channel kilometers are shown by the black circles. The curvilinear grid in the estuary follows the meandering channel and has a cross-channel slope which is maximal at the bend apexes. In the shelf, salt fluxes are calculated across closed arcs bounded to the shoreline (dotted black line).

linearly from 2–40 m from the shoreline to the ocean boundary. Within the estuary, the grid is curvilinear with 15 m along-channel spacing, 16 evenly distributed cross-channel grid cells in the channel, and up to 16 grid cells which expand outwards over the shoal regions, where they exist. In the vertical, 16 stretched layers with higher resolution at the bottom and surface are used. The model was run using a slow (baroclinic) time-step of 1-second for every 32 fast (barotropic) time-steps, and we analyzed the model output at 6-minute intervals.

The geometry of the estuary is an idealization of the meandering planform and intertidal shoals of the North River. The planform shape of the meandering channel was created using a sine-generated function, consistent with typical geometries of meandering rivers (Langbein & Leopold,

1970). The channel width converges exponentially from 100 m at the mouth to 40 m at 18 km, then remains constant upstream. The channel depth, meander wavelength, and meander amplitude all scale with channel width throughout the estuary, based on the self-similar morphology of tidal meanders (Finotello et al., 2020). The channel depth ranges from 2–5 m and the maximum normalized radius of curvature is representative of sharp meanders ($R/B=1$ where B is channel width and R is the radius of curvature). The channel shape is trapezoidal with a cross-channel slope scaled by the local centerline curvature such that the thalweg is deepest at the outside of each bend apex and the cross-channel slope is zero where the channel curvature is zero. Near the mouth, intertidal shoals, which are 0.5 m deep at mean water level, extend laterally from the channel and converge exponentially from a width of 1,000 m at the mouth to the width of the channel (~90 m) at 3 km. Wetting and drying was enabled with a small critical depth of $D_{\text{crit}}=0.01$ m to minimize false dispersion due to trapping of water on the dry grid cells (Warner et al., 2013). Additionally, a constriction is located at 1 km landward from the mouth where the width is reduced from 550 m to 150 m.

Model runs were initialized from rest and forced with semidiurnal tides (12-hour period) at the open ocean boundaries and constant discharge at the river boundary. Salinity was set to 30 psu at the ocean boundaries and 0 psu at the river end, while temperature was set constant everywhere. Radiation boundary conditions were used for the free surface at the river boundary and for the 3-D velocities and turbulent kinetic energy quantities at all boundaries. The $k-\epsilon$ implementation of the generic lengthscale model (Umlauf & Burchard, 2003; Warner et al., 2005) with a stability function by Kantha and Clayson (1994) was used for the turbulence closure. For bottom drag, a bed roughness of $z_0=0.002$ m was used, a value representative of a bed with ripples (Grant & Madsen, 1982). A small, constant horizontal eddy viscosity of 0.1 $m^2\ s^{-1}$ was used for

Table 1. Model runs with varied forcing conditions and related lengthscales. Variables are tidal range at the mouth (H_t), river discharge (Q_f), tidal excursion (L_t) defined by the distance traveled by the 15-psu isohaline, and estuary length (L_e) defined by the tidal mean of the distance between the 2- and 28-psu isohalines.

Run	Description	H_t (m)	Q_f (m^3 s^{-1})	L_t (km)	L_e (km)
1	Spring, Low Flow[a]	3.6	0.84	8.0	7.4
2	Spring, Moderate Low	3.6	2.5	8.1	4.8
3	Spring, Moderate High	3.6	9.4	7.9	4.8
4	Spring, High Flow	3.6	38	6.3	4.0
5	Medium Spring, Low Flow	3.0	0.79	7.0	6.6
6	Medium Spring, Moderate Low	3.0	2.4	7.0	4.9
7	Medium Spring, Moderate	3.0	9.0	7.0	4.9
8	Medium Spring, High Flow	3.0	36	5.6	4.2
9	Medium Neap, Low Flow	2.4	0.77	5.9	5.9
10	Medium Neap, Moderate Low	2.4	2.4	5.8	5.1
11	Medium Neap, Moderate High	2.4	8.8	5.9	4.5
12	Medium Neap, High Flow	2.4	35	4.8	4.5
13	Neap, Low Flow	1.8	0.76	4.7	5.7
14	Neap, Moderate Low	1.8	2.3	4.7	5.6
15	Neap, Moderate High	1.8	8.5	4.9	5.9
16	Neap, High Flow	1.8	33	4.1	5.0

[a]Base case

stability while the horizontal eddy diffusivity was set to zero. The HSIMT tracer advection scheme by Wu and Zhu (2010) was selected to avoid unphysical salinity values near sharp gradients.

The model was forced with a range of river discharges and tidal amplitudes representative of the seasonal and fortnightly variations in the North River estuary (see Table 1 for summary of experiments and forcing parameters). We designate the spring tide, low discharge conditions as the base case as this produces the most well-mixed conditions.

To evaluate the consistency of the model output with a realistic estuary, we compare along-channel salinity profiles from the idealized model to observations from the North River in Figure 2. The salinity profiles were measured during a 2017 field campaign (see Kranenburg et al. 2019 for details), spanning a range of stratification from well-mixed to stratified depending on the river discharge and tidal conditions. The overall salinity structure in the model qualitatively agrees with the observations, though axial salinity gradients in the idealized model are slightly larger than in the North River, possibly owing to unresolved mixing processes due to bathymetric effects.

3 Salt fluxes

3.1 *Eulerian salt flux decomposition*

In an Eulerian frame, the primary mechanisms contributing to the subtidal (tidally averaged) salt balance can be identified by decomposing the salinity, s, and along-channel velocity, u, at a cross-section into multiple components based on a sequence of spatial and temporal averaging (Dronkers & van de Kreeke, 1986; Fischer et al., 1979; Hughes & Rattray, 1980; Lerczak et al., 2006). Following Dronkers and van de Kreeke (1986), we separate each cross-section into a finite number of differential area elements dA which span laterally across the channel and expand/contract vertically with the tides. We then decompose salinity and velocity into three component each: 1) tidally averaged, cross-sectionally averaged; 2) tidally varying,

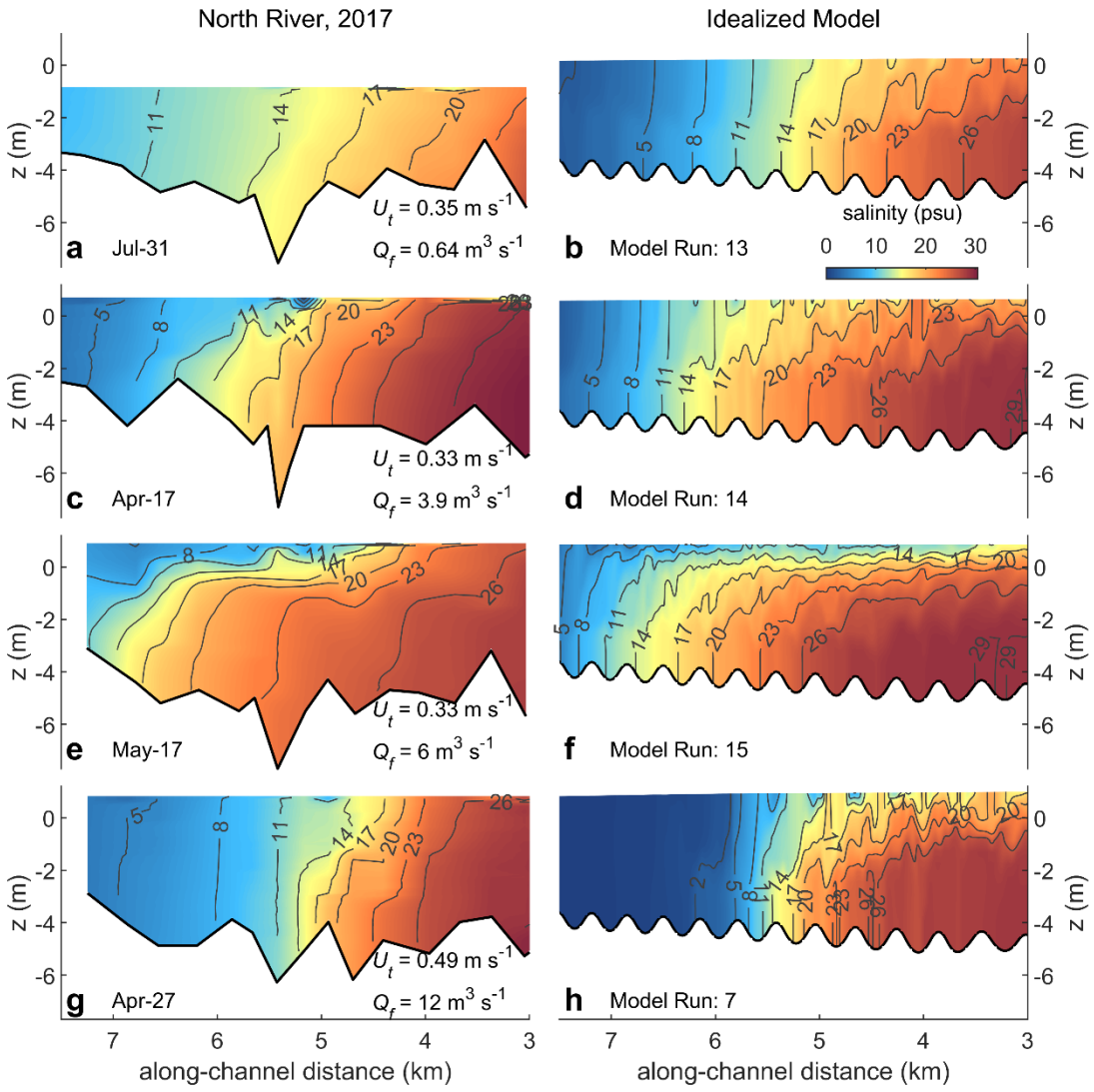

Figure 2. Along-channel salinity profiles in the North River (left) and the idealized model (right) used in this study. The thalweg depth in the model varies based on the local channel centerline curvature and is deepest at bend apexes. The model runs shown have similar forcing conditions and tidal phase as the corresponding observations. Contour interval is 3 psu.

174 cross-sectionally averaged; and 3) tidally varying, cross-sectionally varying. The three salinity
175 components are defined, respectively, as

$$
\begin{aligned}
s_0 &= \langle \overline{s} \rangle, \\
s_1 &= \overline{s} - s_0, \\
s' &= s - s_1 - s_0,
\end{aligned}
\tag{1}
$$

176

177 where angle brackets indicate a tidal average, overbars indicate a cross-sectional average, e.g.,
178 $\overline{s} = A^{-1} \iint s\,dA$, and $A = \iint dA$ is the tidally varying cross-sectional area. The first term, s_0,
179 represents the steady component of the cross-sectional average while the second term, s_1,
180 represents the tidally varying component of the cross-sectional average. The third term, s', is the
181 deviation from the cross-sectional average. From these definitions, it follows that $\langle s_1 \rangle = 0$ and
182 $\overline{s'} = 0$. Velocity is decomposed in an identical manner.

183 We next consider the decomposition of velocity into its analogous components. In order to
184 account for the Stokes transport, we consider the volume transport through a cross-section,
185 $Q = \iint u\,dA$, which we decompose into two components,

$$
\begin{aligned}
Q_0 &= \langle Q \rangle, \\
Q_1 &= Q - Q_0.
\end{aligned}
\tag{2}
$$

186

187 The volume transport is therefore separated into a tidally-averaged term, Q_0, which at steady state
188 is equivalent to the river discharge Q_f, and a tidally varying term, Q_1, which represents the tidal
189 volume transport. Using these decompositions, we obtain an expression for the tidally averaged
190 salt flux through a cross-section:

$$
\begin{aligned}
F &= \langle \iint (u_0 + u_1 + u')(s_0 + s_1 + s')\,dA \rangle \\
&= Q_0 s_0 + \langle Q_1 s_1 \rangle + \langle \iint u' s'\,dA \rangle \\
&= F_0 + F_1 + F_2.
\end{aligned}
\tag{3}
$$

191

192 The terms $F_0, F_1,$ and F_2 represent the three components of the tidally averaged salt flux
193 corresponding to: i) $Q_0 s_0$, the steady advective river outflow; ii) F_1, the tidal oscillatory salt flux
194 due to tidal correlations of the cross-sectionally averaged velocity and salinity; and iii) F_2, the
195 local dispersive salt flux due to spatial correlations of the velocity and salinity over the cross-
196 section through the tidal cycle. At steady state, the net salt flux $F = 0$.

197 The F_2 term, which is the tidally averaged salt flux due to steady and oscillatory shear
198 dispersion (Bowden, 1965; Taylor, 1953), can be further decomposed by separating u', s' into
199 different components. For example, we could separate each into a steady and tidally varying
200 component, the correlation of which corresponds to steady and oscillatory shear dispersion,
201 respectively (Lerczak et al., 2006). However, for examination of the difference between local and
202 nonlocal dispersion, we do not distinguish between the steady and unsteady shear dispersion, but
203 rather consider both as contributions to the local dispersive salt flux F_2. To differentiate between
204 mechanisms of local shear dispersion, we decompose u', s' into their laterally and vertically
205 varying components. For salinity, we define

206
$$\begin{aligned} s_l' &= \frac{\int s_l' dz}{H}, \\ s_v' &= s' - s_l', \end{aligned} \tag{4}$$

207 where z is the vertical coordinate and $H = \int dz$ is the total water depth. The depth averaged
208 component, s_l', varies only over the cross-channel coordinate y and the remaining component,
209 s_v', is the only term including vertical variations. Applying the same decomposition to u', we
210 obtain an expression for the lateral and vertical components of the local dispersive salt flux:

$$
\begin{aligned}
F_2 &= \langle \iint (u_l' + u_v')(s_l' + s_v') dA \rangle \\
&= \langle \int u_l' s_l' H \, dy \rangle + \langle \iint u_v' s_v' dA \rangle \\
&= F_{2l} + F_{2v}.
\end{aligned}
\tag{5}
$$

Here, F_{2l} is the component of the local dispersive salt flux due to correlations of the depth averaged velocity and salinity over the width, while F_{2v} is the component of the local dispersive salt flux due to the remaining vertical correlations between velocity and salinity over the cross-section.

3.2 *DvdK86 moving plane analysis*

To analyze the nonlocal dispersive salt flux and the physics that generate it, we apply the quasi-Lagrangian framework of Dronkers and van de Kreeke (1986), which shall be described here. We define a moving plane which coincides with a fixed cross-section at some time t_0 to be specified below and whose position oscillates with the tides at a velocity of $U_1 = Q_1 / A$. Following the same method applied to the velocities and salinities at a fixed cross-section, we obtain the decomposition of the tidally averaged salt flux through a moving plane,

$$
\begin{aligned}
\tilde{F} &= \tilde{Q}_0 \tilde{s}_0 + \langle \iint \tilde{u}' \tilde{s}' d\tilde{A} \rangle \\
&= \tilde{F}_0 + \tilde{F}_2.
\end{aligned}
\tag{6}
$$

Here, the tilde denotes variables in the moving plane and subscripts are defined in the same way as in the previous section. Since $\tilde{Q}_1 = 0$ by definition of the moving plane, the tidal oscillatory salt flux $\tilde{F}_1$ vanishes, and the only remaining salt flux terms are the steady advective river flux $\tilde{F}_0$ and the local dispersive salt flux $\tilde{F}_2$. For constant river discharge, $\tilde{Q}_0 = Q_0$, and at each stationary cross-section, there exists a time t_0 which can be selected such that in the moving plane, $\tilde{s}_0 = s_0$. At steady state, $F = \tilde{F} = 0$, and thus for a fixed cross-section and its corresponding moving plane,

$$F_1 + F_2 = \tilde{F}_2. \quad (7)$$

The tidal oscillatory salt flux, F_1, is therefore equal to the difference between the local dispersive salt fluxes in the moving and fixed plane, $\tilde{F}_2 - F_2$. Based on this result, Dronkers and van de Kreeke (1986) describe F_1 as the "nonlocal" salt flux, because (7) indicates that F_1 arises due to the spatially varying contributions of "local" shear dispersion that occurred elsewhere within one tidal excursion of a stationary cross-section. Furthermore, this result implies that all dispersive salt flux can be tied to shear dispersion somewhere either in the estuary or adjacent coastal waters.

3.3 *Calculation of salt fluxes and the moving plane*

We calculate the salt flux components at the velocity faces of the model grid. Tidal averages are calculated from the mean value over one tidal period (12-hr) of the model once it reaches steady state, based on when $F \approx 0$ in the estuary. For high flow conditions, this occurs within 1–4 days, and for low flow conditions this occurs after about 7–10 days. At dry grid cell faces, we set the differential area dA to zero. The use of an orthogonal curvilinear grid in the channel facilitates the calculation of the salt flux terms at each cross-section within the channel. We note that the moving planes must extend to solid boundaries to ensure both volume and mass conservation. Thus, in the coastal shelf, we calculate the salt flux terms across closed arcs bound to the shoreline and aligned with the nearest u and v faces of the model grid (see Figure 1).

To calculate the salt fluxes in the moving plane, we start by determining the tidally varying position of the planes, X, for each along-channel location along the estuary. We use a predictor-corrector method to integrate U_1 in time to obtain the position of X over a tidal cycle, beginning at each along-channel location at an arbitrary time in the tide. Then, we interpolate the cross-sectional average values of salinity onto the tidally varying positions of each moving plane.

Afterwards, for each fixed location in the estuary, we select the moving plane with the most similar tidally averaged, cross-sectionally average salinity such that $\tilde{s}_0 = s_0$ for that moving plane and the fixed location. Once the corresponding moving plane for each fixed location is identified, we then interpolate instantaneous values of the local dispersive salt flux, $\iint u's'dA,$ onto the tidally varying positions of X to obtain the instantaneous dispersive salt flux, $\iint \tilde{u}'\tilde{s}'dA,$ as well as its lateral and vertical components. Finally, we take the tidal average to determine $\tilde{F}_2, \tilde{F}_{2l}, \tilde{F}_{2v}$.

4 Results

4.1 *Subtidal and instantaneous salt fluxes*

A comparison of the salinity and salt fluxes in the Eulerian (fixed) and moving planes for the base case (spring tide, low flow) is shown in Figure 3. Each along-channel position can be mapped to the moving plane having the same tidally averaged salinity (Figure 3a,b). While salinity at the fixed positions can span nearly the entire range from fresh to oceanic salinity at the central region of the distribution, the salinity in the moving planes is nearly constant. This indicates that for these forcing conditions, the moving planes follow nearly the same trajectory as the isohalines, though this is not necessarily true for other conditions, such as high river flow.

For the Eulerian salt flux decomposition (Figure 3c), the steady advective salt flux – which conforms to the shape of the salinity distribution since the river discharge is constant – is balanced by the sum of the nonlocal (F_1) and local dispersive (F_2) salt fluxes, both of which are highly variable along the channel. In the coastal region outside the mouth (<0 km), the nonlocal term becomes small while the local term is large, indicating locally enhanced shear dispersion. At the constriction (1 km), there is a peak in the local dispersive salt flux on either side of the constriction. Because the local term on the landward side of the constriction exceeds the steady advective term,

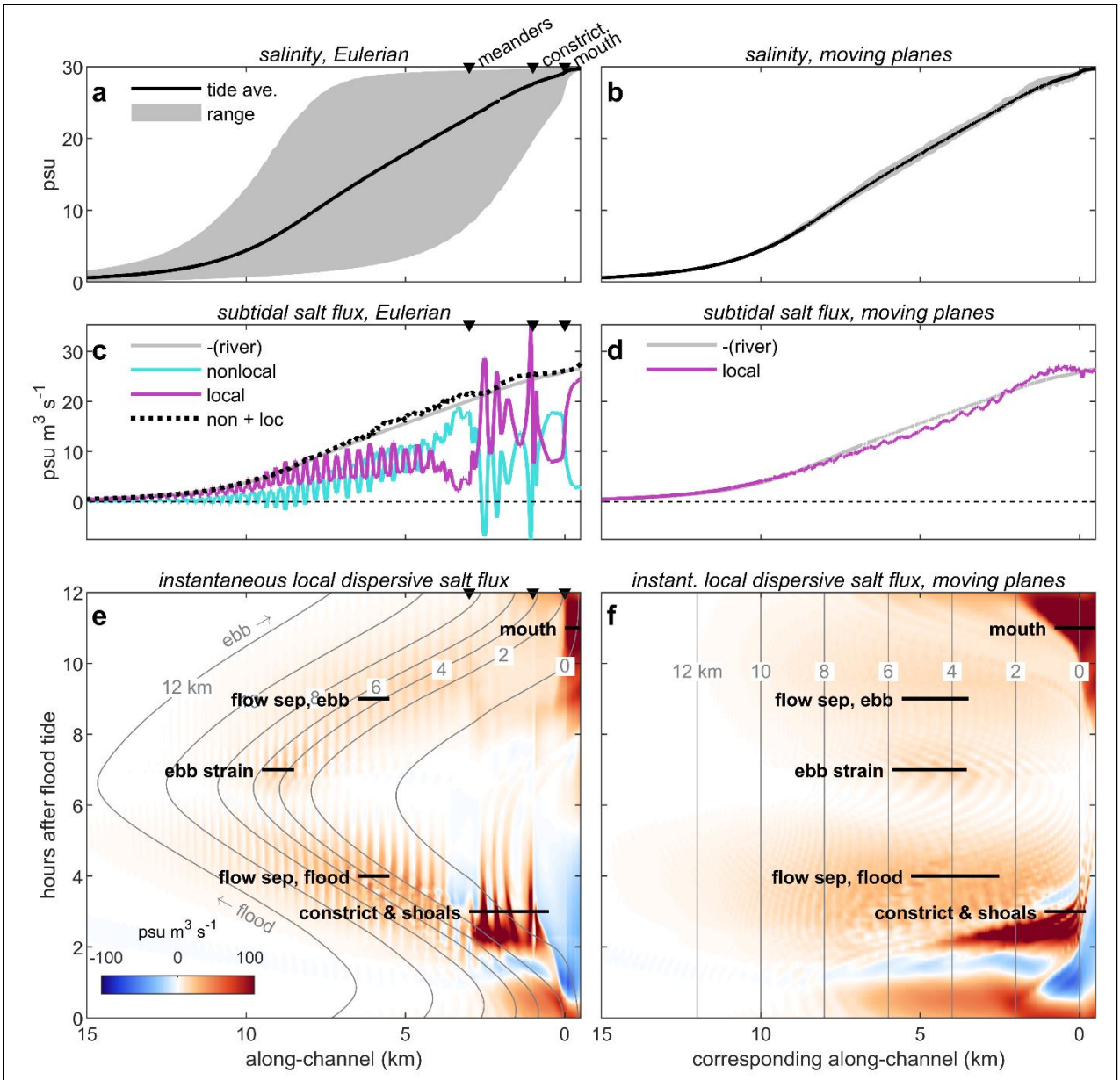

Figure 3. Comparison between salinity and salt fluxes in the Eulerian (left) and moving (right) frames. (a,b) Tidally averaged salinity (black) and tidal salinity range (grey shading). (c,d) Salt flux decomposition: river flow (grey), nonlocal salt flux (cyan), local dispersive salt flux (purple). The river flow is balanced by the sum of the nonlocal and local dispersive salt flux (black dashed line) in the Eulerian frame, whereas it is entirely balanced by the local dispersive salt flux in the moving plane. (e,f) Instantaneous local dispersive salt flux in the estuary over a tidal cycle (red landward, blue seaward), starting at the beginning of flood tide at the mouth (0 km). The paths of the moving planes at every 2 km are shown by the grey lines in (e), corresponding to the vertical grey lines in (f). The black labeled lines in (e,f) highlight the hotspots of dispersion shown in Figure 4, Figure 5, Figure 6, and Figure 7.

the nonlocal term must be negative to conserve salt. However, at the center of the constriction where the cross-section is smallest, the nonlocal salt flux must increase to compensate for the reduction in the local dispersive salt flux. Beyond the constriction in the channel-shoal region (1–3 km), the landward salt flux results primarily from the local term which exhibits along-channel variability due to the meandering geometry. The nonlocal salt flux is largest just landward from the end of the channel-shoal region (3–4 km), where the local dispersive salt flux is weakest. Upstream in the channel (>4 km), both the local and nonlocal terms contribute similarly to landward salt flux and alternate in magnitude with spatial variability related to the lengthscale of the meanders. For the moving planes, however, the river flow is entirely balanced by the local dispersive salt flux (Figure 3d).

To obtain insight into the subtidal salt balance, we next consider the instantaneous local dispersive salt flux, $\iint u's'dA$, both in the fixed Eulerian coordinates and the transformed coordinates defined by the quasi-Lagrangian moving planes (Figure 3e,f). The tidally averaged local dispersive salt flux terms in both Figure 3c and d are obtained by averaging the instantaneous dispersive salt flux along a vertical line in Figure 3e and f, respectively. Note that because the corresponding along-channel position of the moving planes is not defined by its tidally averaged position but rather by matching its tidally averaged salinity to a fixed location, the along-channel spacing between individual moving planes does not remain constant over a tidal cycle. The transformation of the along-channel coordinate from the Eulerian frame to the quasi-Lagrangian DvdK86 moving frame thus involves both a translation as well as an expansion/contraction in space.

The instantaneous local dispersive salt flux exhibits strong spatiotemporal variability. Compared to the tidally averaged dispersive salt flux, which reaches a maximum value of ~30 psu

298 $m^3 s^{-1}$ at the seaward limit of the estuary, the instantaneous dispersive salt flux can an order of
299 magnitude larger. In the Eulerian frame, the instantaneous dispersive salt flux reaches values of
300 ~150–250 psu $m^3 s^{-1}$ near the mouth (<0 km) around hour 12 and at the constriction and channel-
301 shoal region (0–3 km) at hour 3. Enhanced dispersion also occurs in the meandering channel (>3
302 km) at hours 4, 7, and 9, reaching a maximum magnitude of ~60 psu $m^3 s^{-1}$. As shown by the
303 DvdK86 moving planes analysis, the locally enhanced dispersive salt flux occurring in these
304 regions contributes to the nonlocal salt flux in other parts of the estuary. In the following
305 subsections, we explore these "hotspots" of local shear dispersion, as these are the main sources
306 of the landward salt flux in the estuary.

307 #### 4.1.1 NEAR MOUTH REGION

308 The region near the mouth becomes highly dispersive during late ebb, as indicated in
309 Figure 3e,f. The mechanisms causing this strong dispersion are illustrated in Figure 4. The large
310 lateral dispersive salt flux outside the mouth results from the jet-like outflow from the estuary,
311 which has significantly higher momentum and lower salinity than the ambient coastal water.
312 Within ~750 m from the mouth, the outflow is nearly well-mixed and the vertical dispersive flux
313 is small while the lateral dispersive flux due to lateral flow separation is large. As the depth
314 increases beyond this point, the buoyant outflow detaches from the bottom. Beyond the liftoff
315 point, the outflow becomes stratified and vertically sheared, corresponding to the enhancement of
316 vertical shear dispersion away from the mouth. As the outflow becomes stratified, it also spreads
317 radially, which reduces lateral variations in salinity and thus decreases lateral shear dispersion.
318 Thus, the mouth region acts as a source of both lateral and vertical shear dispersion. Given that the
319 changes in depth and width typically associated with estuary mouths enable both lateral flow

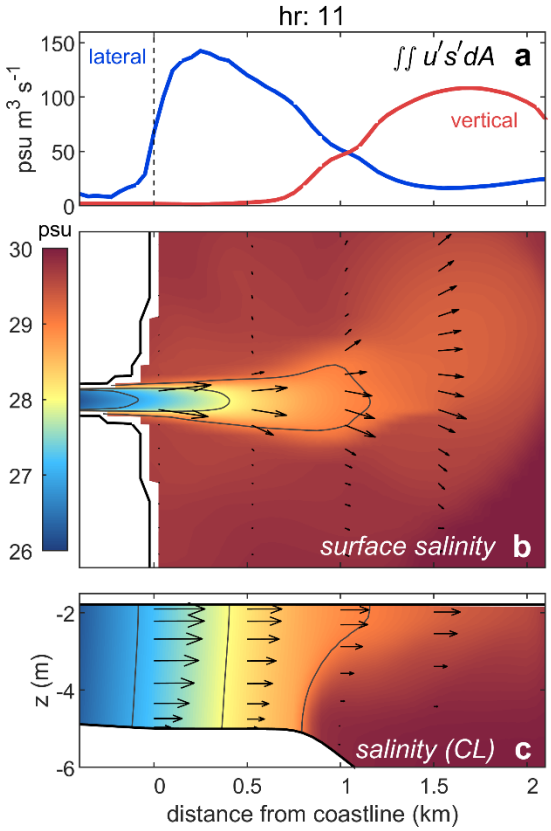

Figure 4. Dispersion near the mouth during late ebb tide, hours 11. (a) Instantaneous values of the lateral (blue) and vertical (red) local dispersive salt flux along the channel. (b) Plan view of the surface salinity and surface velocity vectors. (c) Salinity profile along the centerline of the estuary and adjacent coastal shelf. Contour interval is 1 psu.

separation and strong vertical straining, the mouth is therefore an important source of dispersion for many estuaries.

4.1.2 Constriction and Shoals

Significant dispersion also occurs during flood tide near the constriction at 1 km from the mouth and in the adjacent channel-shoal region (Figure 5). In this region, the primary mechanisms of dispersion are jet-sink exchange at the constriction (Stommel & Farmer, 1952) and tidal trapping

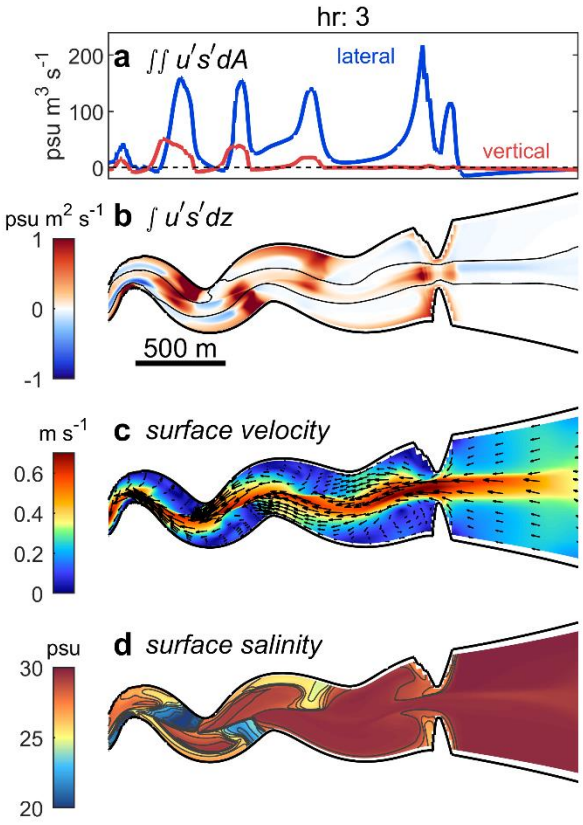

Figure 5. Jet-sink exchange and tidal trapping in the channel-shoal region during maximum flood, hour 3. (a) Instantaneous values of the lateral (blue) and vertical (red) local dispersive salt flux along the channel. (b) Depth-integrated instantaneous local dispersive salt flux. The black line indicates where the velocity is equal to the cross-sectionally averaged velocity, which separates the fast-flowing water in the channel from the slow water over the shoals. (c) Surface velocity magnitude with velocity vectors. Note the jet-like flow and the corresponding flow separation on the downstream side of the constriction. (d) Surface salinity contours at 1 psu intervals.

in the shoals (Okubo, 1973). On the upstream side of the constriction, the flow pattern is like a sink flow which funnels into the constriction. Downstream of the constriction, the fast currents produce a jet, which remains separated from the water on the shoals due to the adverse pressure gradient in the expansion. Because the currents in the channel are much stronger than in the shoals, differential advection during flood tide increases the salinity difference between the channel and

the shoals such that the channel is saltier, resulting in a landward dispersive salt flux. The velocity and salinity structure are also impacted by the curving planform, the effects of which will be described in the following section on the meanders. During ebb tide, differential advection downstream from the constriction would cause the channel to be fresher, which also contributes to a landward dispersive salt flux. However, due to the partially progressive characteristics of the tidal wave, maximum currents during ebb tide do not occur until after the intertidal shoals have already become dry – therefore, strong lateral shear dispersion in this region is present only during the flood tide.

4.1.3 Flow separation in the meanders

Landward from the channel-shoal region of the estuary, the local dispersive salt flux in the channel is punctuated spatially by the presence of meander bends, which introduce an axial lengthscale of variability to the velocity, salinity, and dispersive salt flux (Figure 6). The local maxima in dispersive salt flux occurs on the downstream side of the bend apexes during both flood and ebb, coinciding with the locations of a flow separation zone. In the meanders, the streamwise velocity is largest at the inside of the bend, owing to the effects of channel curvature (potential vortex flow) and the absence of any significant inner channel bar to redistribute momentum (Blanckaert, 2010; Kranenburg et al., 2019). This maximal inner bend velocity creates areas of low pressure on the inside of the bend, resulting in adverse pressure gradient downstream of the bend apex and thus flow separation (Bo & Ralston, 2020). These flow separation zones function as dead zones or "traps" (Okubo, 1973), where, during flood tide, these slow – or recirculating – regions remain relatively fresher than the fast-flowing regions in the channel and during ebb tide, these flow separation zones remain relatively saltier. Furthermore, the flow separation zones are the only regions in the meanders which sustain significant stratification. This is because the lateral

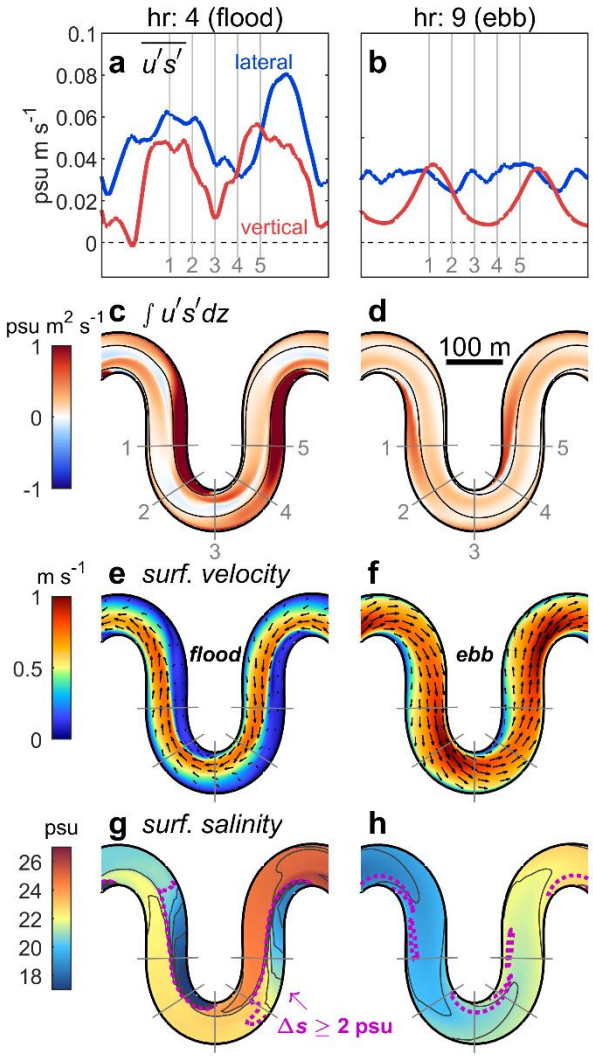

Figure 6. Flow separation in the meanders during (left) maximum flood, hour 4, and (right) maximum ebb, hour 7. (a,b) Instantaneous cross-section averaged values of the lateral (blue) and vertical (red) local dispersive salt flux along the channel. (c,d) Depth-averaged instantaneous local dispersive salt flux, with transects corresponding to the vertical lines in (a,b). The solid black line indicates where velocity is equal to the cross-sectional average. (e,f) Surface velocity magnitude and velocity vectors, showing a marked transverse shear where the flow is fastest on the inside of the bend. (g,h) Surface salinity at 1 psu intervals, with stratified regions ($\Delta s \geq 2$ psu) delineated by the magenta dotted line.

355 salinity difference across the flow separation zone is about 5 psu during flood tide and about 3 psu
356 during ebb. These lateral salinity gradients, in combination with stagnant flow in the separation
357 zone, drive a baroclinic circulation that stratifies the separation zone.

358 The dispersive salt flux is stronger during flood tide than ebb tide, even when accounting
359 for differences in the cross-section area (Figure 6a,b). One reason is that flow separation tends to
360 be stronger during flood tide than ebb tide because of its dependency on water depth (Bo &
361 Ralston, 2020). Differences in secondary flow patterns also affect the intensity of the flow
362 separation. The transverse baroclinic circulations in the flow separation zone impact the flow
363 patterns at the downstream bend apex by enhancing the curvature-induced secondary flow
364 (outward at the surface, inward at depth, e.g. Rozovskii 1957) during ebb tide and counteracting it
365 during flood. In fact, during flood tide a reversed lateral circulation cell (inward at the surface,
366 outward at depth) can be observed on the outside of the bend, consistent with the observations of
367 Kranenburg et al. (2019) in the North River. This reversed lateral circulation during flood tide
368 inhibits the curvature-induced secondary flow from redistributing the high momentum fluid inside
369 the bend towards the outside of the bend. The enhanced lateral shear during flood tide thus
370 corresponds to stronger dispersion compared to ebb. In addition to differences in water depth and
371 secondary circulation patterns from flood to ebb tide, a larger axial salinity gradient during flood
372 tide compared to ebb tide (to be discussed in section 4.2) also contributes to enhanced dispersion
373 as the axial salinity gradient is ultimately transformed into cross-sectional variations in salinity.

374 #### 4.1.4 EARLY EBB TIDE STRAINING

375 During early ebb tide (Figure 7), the local dispersive salt flux in the meanders is due
376 primarily to the tidal straining mechanism (Simpson et al., 1990). Along the meanders, the
377 dispersion is dominated by vertical shear and stratification which are maximal on the upstream

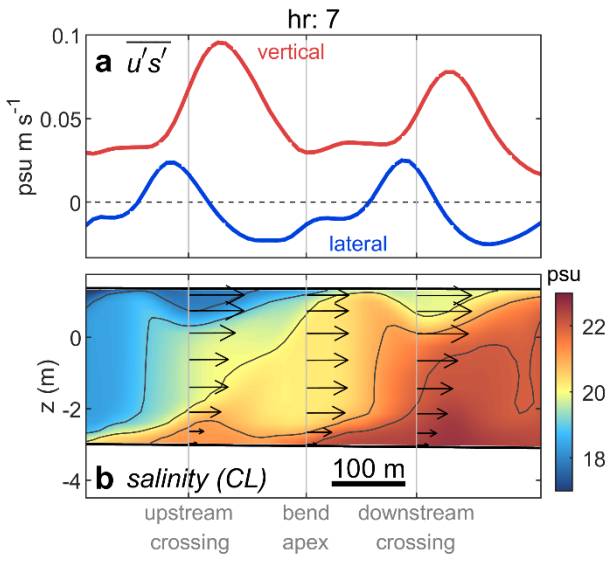

Figure 7. Tidal straining along a meander during early ebb, hour 7. (a) Instantaneous cross-section averaged values of the lateral (blue) and vertical (red) local dispersive salt flux along the channel. (b) Salinity profile along the channel centerline. Contours intervals are 1 psu. The location of the transects corresponding to the upstream crossing, bend apex, and downstream crossing are labeled and highlighted by the vertical lines in light grey.

(landward) side of each bend apex. This stratification initially results from the relaxation of lateral salinity gradients that were setup on the landward side of the bend apexes during the flood tide. Because of the reduced turbulent mixing due to stratification, the along-channel velocity becomes vertically sheared once the tide reverses and the ebb begins (Stacey et al., 2001). This vertically sheared along-channel velocity strains the along-channel gradient to produce even more stratification. Thus, the lateral salinity variations caused by flow separation in the meanders during flood tide act to prime the tidal straining mechanism at the beginning of ebb, thereby enhancing the vertical component of the local dispersive salt flux on the landward side of the bend apexes. As along-channel velocity shear continues to increase, however, secondary circulations due to the flow curvature locally enhance mixing, especially at the bend apex where stratification and the local dispersive salt flux are reduced.

4.2 *Along-channel salinity gradient*

It is important to note that the presence of an along-channel salinity gradient is necessary for the dispersive salt flux because cross-sectional variations in salinity result from straining of the along-channel gradient. In short estuaries, the instantaneous salinity gradient can vary by over an order of magnitude along the estuary and at different phases of the tide. Therefore, we next consider the spatiotemporal variation of the salinity gradient for the base case (spring tide, low flow), as well as for three other forcing conditions corresponding to the other limits of the simulated parameter space: neap tide, low flow; spring tide, high flow; and neap tide, high flow.

The instantaneous cross-section averaged salinity gradient, $\partial \overline{s} / \partial x$, has a nearly Gaussian along-channel distribution and varies in magnitude, shape, and position through the course of a tidal cycle (Figure 8). For all cases, the longitudinal lengthscale of the peak salinity gradient is significantly smaller than the tidal excursion. As a result, the tidally varying position of the high-gradient zone causes strong dispersion to occur at different places along the estuary throughout the tidal cycle. At the beginning of flood tide (hour 0), the maximal salinity gradient usually occurs at the seaward end of the salinity distribution – near the mouth except for the neap, low flow regime. Dispersive processes – especially during the late flood through early ebb (hours 4 to 7) – cause the peak salinity gradient to relax, resulting in the peak salinity gradient being smaller during the ebb tide than for flood and thus contributing to flood-ebb asymmetries in the magnitude of the dispersive salt flux. Through ebb tide, the salinity distribution is advected back towards the coastal ocean, where it is subjected to strongly frontal conditions that regenerate the maximal salinity gradient before the ensuing flood tide.

Variations in forcing conditions contribute to changes in both the shape and along-channel position of the high gradient zone of the salinity distribution over the tidal cycle, thus determining

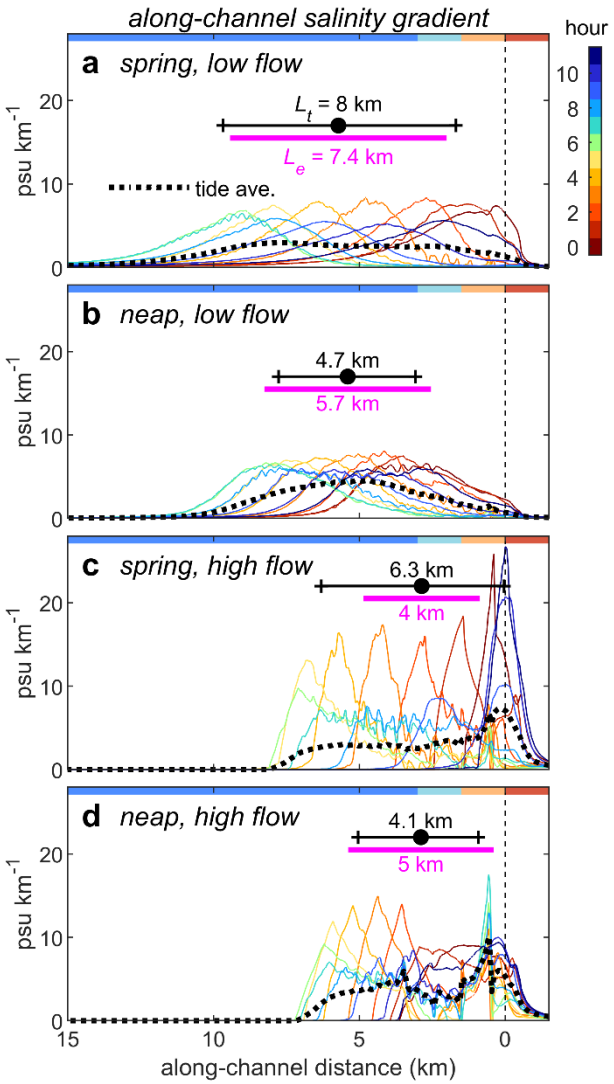

Figure 8. Along-channel salinity gradient at 1-hour intervals after beginning of flood tide for (a) spring tide, low flow, (b) neap tide, low flow, (c) spring tide, high flow, and (d) neap tide, low flow. The tidally averaged salinity gradient (black dotted line) has a smaller, wider peak than the instantaneous distributions. The tidal excursion length L_t based on the position of the 15-psu isohaline is shown by the black line and the tidal mean position of the 15-psu isohaline is shown by the black circle. The estuarine length L_e based on the tidal mean distance between the 2- and 28-psu isohalines is shown by the magenta line. A 1-km moving box filter was applied to the along-channel salinity gradient. Bars along the top of each plot correspond to the along-channel geographic range of each of the regions of the estuary as defined in Figure 9.

when and where shear dispersion takes place. In addition to enhancing the along-channel salinity gradient, higher river flows also shift the zone of maximum gradient seaward towards the mouth. Additionally, the strength of the tidal currents determines the spatial extent over which the salinity distribution is advected. Notably, under spring tides, high flow conditions (Figure 8c), the maximum salinity gradient is advected past the mouth of the estuary, resulting in a sharp enhancement of the gradient at the end of ebb tide.

We note that the tidally averaged along-channel salinity distribution does not resemble the instantaneous salinity distribution at any point in the tidal cycle. The peak instantaneous along-channel salinity gradient is typically 2–3 times larger than the peak tidally averaged salinity gradient, and it is more sensitive to variations in discharge than the tidal average gradient. During all conditions but particularly during the spring tide, high flow case, as the lengthscale of the estuarine salinity distribution, L_e, is shorter than the tidal excursion length, L_t, so tidal averaging of $\partial\overline{s}/\partial x$ obscures its strength and spatial structure. The disparities between the instantaneous and tidally averaged distribution of $\partial\overline{s}/\partial x$ suggest that for short estuaries where $L_e \sim L_t$, the tidally averaged salinity gradient has little dynamical significance.

4.3 *Spatial variations in dispersion*

In this section, we utilize the DvdK86 method to quantify the dispersive salt fluxes associated with topographic features and show where this dispersion affects the salt balance throughout the estuary. By analyzing the salt fluxes through the DvdK86 moving planes, we can attribute the total dispersive salt flux at each fixed section to the shear dispersion from other regions of the estuary based on when the moving planes corresponding to those fixed locations pass through each region. We separate the estuary along the channel into 4 main regions based on topographic features: the mouth, the constriction, the shoals, and the meandering channel. Then,

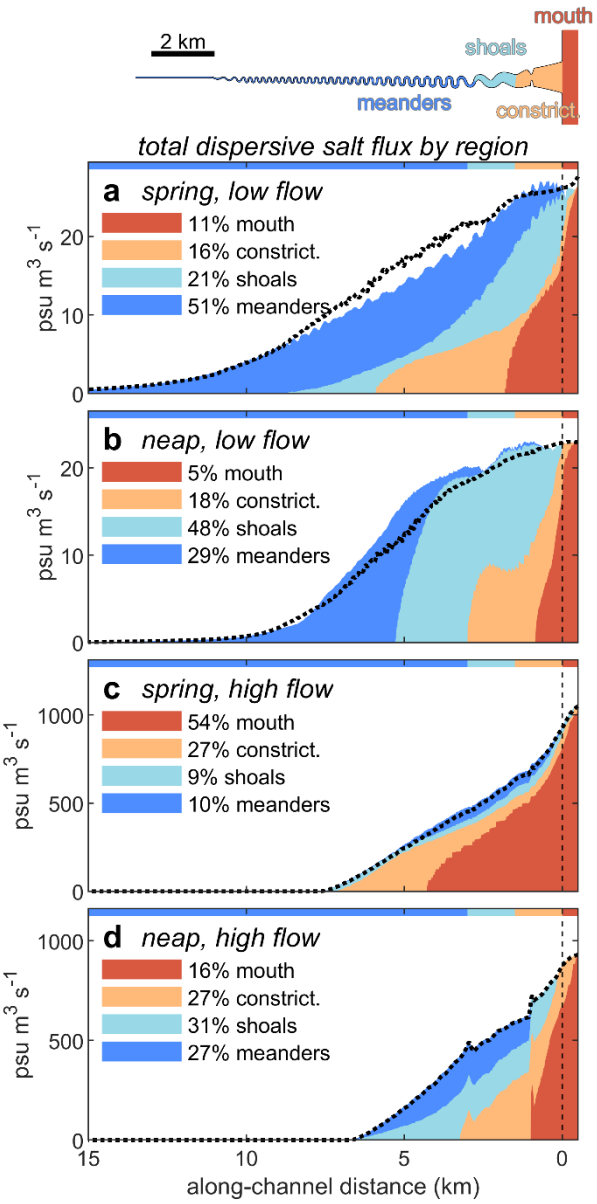

Figure 9. Contributions to the total dispersive salt flux based on the salt fluxes through the moving planes as they pass through each geographic region as defined by the different colors on the map at the top. Different forcing conditions are (a) spring, low flow, (b) neap, low flow, (c), spring, high flow, and (d) neap, high flow. The color bars along the top of each plot corresponds to the along-channel geographic range of each of the regions. The sum of the nonlocal and local dispersive salt fluxes through the fixed locations is shown by the black dashed line. Percentages are calculated from along-channel integrals of the dispersive salt flux inside the estuary (>0 km).

we integrate in time the instantaneous dispersive salt flux through the moving planes over the periods that they pass through each region. To obtain tidally averaged salt flux contributions for each region, we take the integral quantities corresponding to the different regions and divide each by the tidal period.

In Figure 9, we show the contributions of dispersion from each fixed region as they are nonlocally distributed to other parts of the estuary over the scale of a tidal excursion. Under the various forcing conditions, the resulting changes in the relative contributions of dispersion from each region reflects not only the importance of different mechanisms of dispersion but also the position of the gradient zone of the salinity distribution relative to each region. For the base case (spring, low flow, Figure 9a), dispersion within the meander region is the largest contributor to the total dispersive salt flux. Since we have observed under these forcing conditions that the instantaneous dispersive salt fluxes near and outside the mouth are greater than those in the meandering channel region of the estuary, the relative dominance of dispersion in the meanders indicates that the salinity distribution spends the greatest fraction of the tidal cycle in this region. For neap tide, low flow conditions (Figure 9b), flow separation in the meanders becomes relatively less important to the total dispersive salt flux compared to dispersive processes in the shoals region of the estuary. This results from both weaker flow separation in the meanders due to smaller tidal currents as well as the gradient zone of the salinity distribution spending a relatively greater fraction of the tidal cycle downstream in the shoals region. At higher river discharge cases (Figure 9c,d), the magnitude of the dispersive salt flux correspondingly increases. We note that for spring tide, high flow (Figure 9c), more than half of the dispersive salt flux originates from dispersion outside the mouth of the estuary. This result highlights the connection between dispersive

processes near the mouth and the salt balance of short, tidally dominated estuaries in which the peak salinity gradient may spend a significant portion of the tide in the vicinity of the mouth.

4.4 *Lateral vs. vertical shear dispersion*

We can also use the DvdK86 method to distinguish the total dispersive salt flux between lateral and vertical shear dispersion (Figure 10). For the base case of spring tide and low discharge conditions (Figure 10a), lateral shear dispersion is the primary mode of dispersive salt transport throughout the estuary. Under neap tide and low discharge conditions (Figure 10b), however, the dispersive regime transitions to an intermediate one with lateral shear dispersion dominating near the mouth and vertical shear dispersion dominating upstream in the channel. This indicates that lateral flow separation in the meanders is weak under neap tide conditions, while vertical shear dispersion due to early ebb tide straining still contributes significantly to the salt balance. At high river discharge conditions (Figure 10c,d), vertical shear dispersion, resulting from vertical flow separation at the mouth as well as baroclinic exchange flows, accounts for the majority of the dispersive salt flux.

5 Discussion

5.1 *Why does dispersion occur in hotspots?*

In contrast to the classical notion of a steady estuarine circulation driving the landward salt flux over the length of the estuary, we find that in this model of a short, tidally dominated estuary, most of the dispersive salt flux occurs at hotspots in both space and time. Furthermore, flow separation and tidal straining are the key processes leading to these instances of locally enhanced shear dispersion. Flow separation occurs downstream of channel expansions, such as the mouth, constrictions, and sharp meander bends, when tidal currents are strong. Tidal straining is most

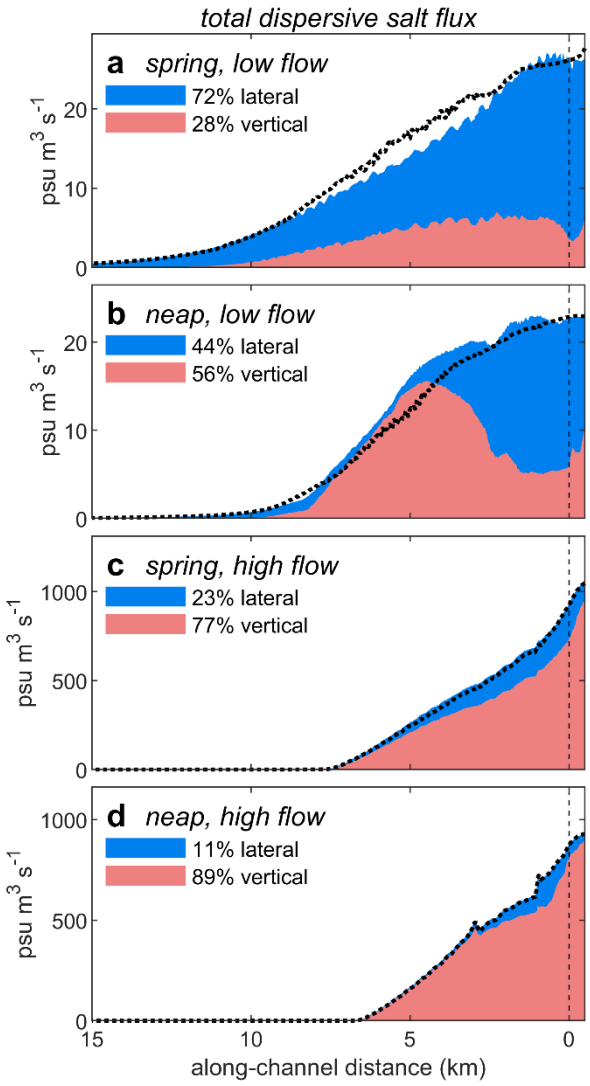

Figure 10. Lateral (light blue) and vertical (light red) components of the local dispersive salt flux through the moving planes corresponding to (a) spring, low flow, (b) neap, low flow, (c), spring, high flow, and (d) neap, high flow. The sum of the nonlocal and local dispersive salt fluxes through the fixed locations is shown by the black dashed line. Percentages are calculated from along-channel integrals of the dispersive salt flux inside the estuary (>0 km).

dispersive around slack tide when tidal currents – and thus mixing – are weak, enabling the development of a vertically sheared, density-driven exchange flow. These mechanisms are important for dispersion because they produce strongly sheared – and often inflected – velocity profiles, which strain the along-channel salinity gradient to create salinity variations over the cross-section. The dispersive salt flux increases with the magnitudes of the velocity shear and corresponding salinity variations, as well as the correlation between them. Therefore, the dispersive salt flux results from the tidal variation of both the tidal currents and the position of the salinity gradient zone with respect to topographic features.

5.2 *How does spatially varying dispersion cause oscillatory salt flux?*

By invoking the moving plane framework of DvdK86, we have shown that the nonlocal salt flux at a fixed location arises due to the variability of shear dispersion within a tidal excursion. Here, we also consider how along-channel convergences in the local dispersive salt flux contribute to the tidal oscillatory salt flux term in the Eulerian frame by shifting the tidal phase between the cross-section averaged velocity and salinity out of quadrature. For example, consider the local maximum in the dispersive salt flux which occurs outside the mouth at the end of ebb. Because the cross-section averaged velocity, $\overline{u}$, is small near slack tide, the contribution of the cross-sectionally averaged advective term becomes small, and therefore the time variation of the cross-section averaged salinity depends mainly on the along-channel convergence of the instantaneous local dispersive salt flux. Landward of the local maximum in the dispersive salt flux at the mouth, the cross-section averaged salinity must increase to conserve salt. Because $\partial\overline{u}/\partial t$ is close to its maximum at slack tide, the positive contribution to $\partial\overline{s}/\partial t$ by the convergence of dispersive salt flux therefore shifts the cross-section averaged salinity slightly into phase with velocity, thus producing a net landward salt flux due to the tidal correlation. In general, regions of maximum

local dispersive salt flux will always cause a relative phase shift so as to cause negative nonlocal salt flux in the regions of maximum local salt flux and positive nonlocal salt flux in adjacent regions.

5.3 *Scaling the mechanisms of dispersion*

The spatiotemporal variability of dispersion suggests that in order to evaluate how individual mechanisms of dispersion vary under different conditions, we must use local instantaneous variables to characterize the local forcing that drives dispersion. In this section, we use multivariate linear regression to determine how the instantaneous dispersive salt flux due to flow separation – a lateral mechanism – and tidal straining – a vertical mechanism – depends on the local instantaneous forcing variables, namely, the cross-section averaged velocity, $\bar{u}(x,t)$, and the along-channel salinity gradient, $\partial\bar{s}(x,t)/\partial x$.

5.3.1 FLOW SEPARATION

For flow separation at the mouth, constriction, and meanders, the lateral shear dispersion increases with larger velocities (Figure 11). At the mouth, the instantaneous dispersive salt flux scales empirically as

$$\overline{u_l' s_l'} \sim \bar{u}^{1.1}\left(\frac{\partial\bar{s}}{\partial x}\right)^{0.7}. \tag{8}$$

We compare this scaling with a general expression for steady shear dispersion in turbulent flows,

$$\overline{u's'} \sim \bar{u}l\left(\frac{\partial\bar{s}}{\partial x}\right), \tag{9}$$

where l is a transverse lengthscale (Elder, 1959; Taylor, 1954). The resemblance between our empirical result and the expression in (9) suggests a quasi-steady state balance between differential advection due to lateral shear and turbulent transverse mixing at the mouth.

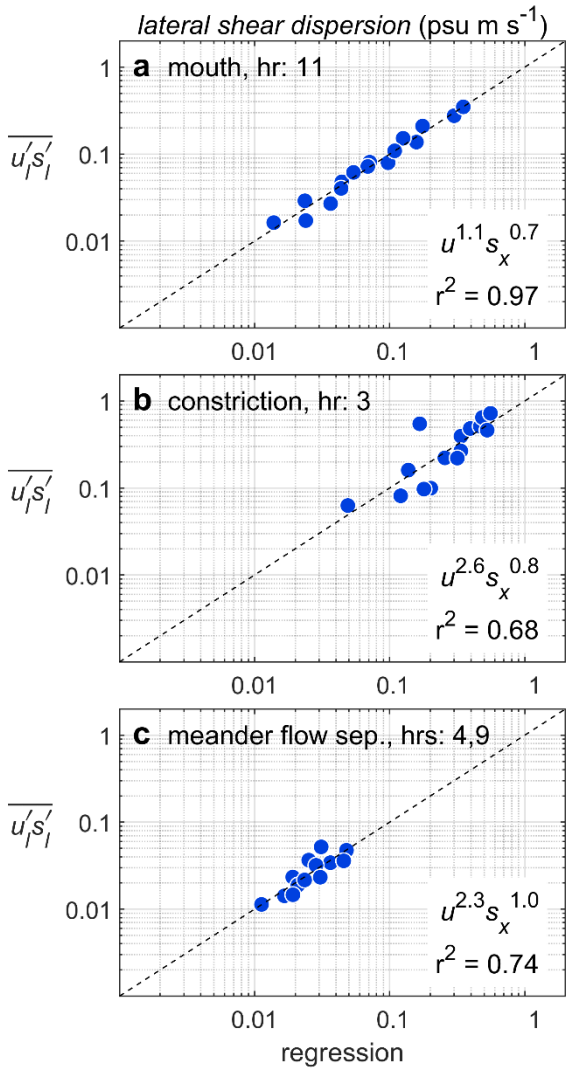

Figure 11. Empirical scaling relationships for the instantaneous dispersive salt flux for lateral flow separation at (a) the mouth, (b) the constriction, and (c) the meanders. The dotted black line is unity. Representative values of the salt flux, cross-section averaged velocity, and salinity gradient were averaged temporally (1-hour) and spatially (400 m) over the associated times and locations: mouth (hour 11, –0.2 km), constriction (hour 3, 1.2 km). For flow separation in the meander regions (hours 4 and 9), a meander length is chosen based on the instantaneous location of the 15-psu isohaline (near the maximum salinity gradient) over the distance from one bend crossing to the next (300 – 400 m). Only low and moderate low flow conditions are shown for the meanders since lateral flow separation is inhibited by stratification at higher flow conditions.

For lateral flow separation at the constriction and meanders, we find a significantly larger exponent for velocity scaling. At the constriction, the instantaneous dispersive salt flux scales as

$$\overline{u_l' s_l'} \sim \bar{u}^{2.6} \left(\frac{\partial \bar{s}}{\partial x} \right)^{0.8}, \tag{10}$$

and in the meanders, it scales as

$$\overline{u_l' s_l'} \sim \bar{u}^{2.3} \left(\frac{\partial \bar{s}}{\partial x} \right)^{1.0}. \tag{11}$$

These strong velocity dependencies suggest that mixing is insufficient to balance straining for flow separation in these locations. In the case of zero mixing, the lateral salinity variations would grow over time due to straining and the dispersive salt flux would scale as

$$\overline{u' s'} \sim \bar{u}^2 \omega^{-1} \left(\frac{\partial \bar{s}}{\partial x} \right), \tag{12}$$

where ω is the tidal radian frequency (Geyer et al., 2008). The similarity between the scaling in (12) and our empirical results for the constriction and meanders may reflect both weak mixing as well as the unsteady nature of the local salinity field due to the dominant role of advection and the short lengthscale of the salinity distribution. While weak mixing might suggest that lateral flow separation results in reversible straining, we note that the salinity variations created at the flow separation can be mixed in other regions of the estuary as they are advected downstream, thus ensuring that the shear dispersion due to flow separation is an irreversible mixing process.

Our results highlight the important role of tidal currents on lateral flow separation, given that the cross-section averaged velocity increases primarily with tidal forcing. Additionally, we note that the nearly linear scaling with the along-channel salinity gradient from the empirical results indicates that lateral flow separation provides a mechanism for enhancing dispersion which is independent of baroclinic processes.

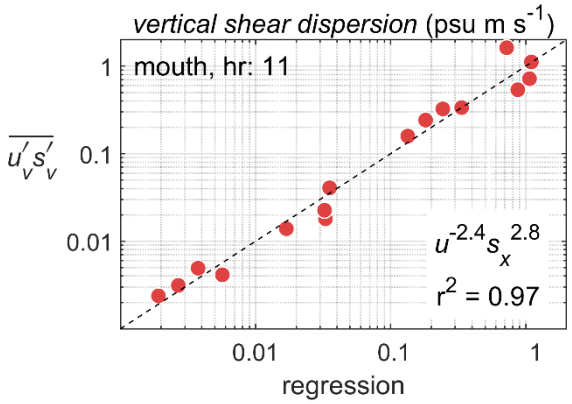

Figure 12. Empirical scaling relationship for the instantaneous dispersive salt flux due to tidal straining at the mouth. The dotted black line is unity. Representative values of the salt flux, cross-section averaged velocity, and salinity gradient were averaged temporally (1-hour) at hour 11 and spatially (400 m) at an along-channel distance of 0.2 km outside the mouth.

5.3.2 TIDAL STRAINING

In contrast to dispersion due to lateral flow separation, the vertical shear dispersion due to tidal straining at the mouth decreases with larger currents and depends more strongly on the along-channel salinity gradient (Figure 12). Here, the instantaneous dispersive salt flux scales as

$$\overline{u_v' s_v'} \sim \bar{u}^{-2.4} \left(\frac{\partial \bar{s}}{\partial x} \right)^{2.8}. \tag{13}$$

We note that this empirical scaling for instantaneous dispersive salt flux is similar to the salt flux due to the steady estuarine circulation,

$$\overline{u's'} \sim U_t^{-3} \left(\frac{\partial s_0}{\partial x} \right)^{3}, \tag{14}$$

where U_t is the tidal velocity amplitude and $\partial s_0 / \partial x$ is the tidally averaged, cross-section averaged along-channel salinity gradient (MacCready & Geyer, 2010). The similarity between our empirical result and the expression in (14) suggests that baroclinicity and strain play the same role in this

559 regime as in the steady estuarine balance to generate the net salt flux, and that the role of the
560 instantaneous currents is mainly to weaken the vertical gradients and thus reduce the salt flux.

561 We note that tidal straining in the meandering channel at the start of the ebb tide also
562 contributes to the landward salt flux. However, unlike at the mouth, we were unable to determine
563 robust scaling relationships between local variables and the dispersive salt flux due to straining in
564 the meanders. This likely results from the fact that the instantaneous stratification is controlled by
565 a combination of processes including axial straining, curvature-induced lateral circulation, and
566 vertical mixing, all of which play varying roles under different forcing conditions.

567 5.4 *Transition from lateral to vertical shear dominance*

568 Given the various mechanisms of dispersion prevalent in this estuary, it is of value to
569 address the relative importance of vertical vs. lateral shear dispersion to the overall salt balance
570 across the various model runs (Figure 13). We quantify the relative strength of baroclinic processes
571 to vertical mixing via the Richardson number (Fischer, 1972) as defined by $\mathrm{Ri}_e = \beta g \Delta s U_f / U_t^3$
572 where β is the coefficient of haline contraction, Δs is the salinity difference between fresh and
573 saltwater, U_f is the freshwater velocity, and U_t is the tidal velocity amplitude. For the base case
574 (spring, high flow) with a small Ri_e, the landward salt flux is driven primarily by lateral shear
575 dispersion processes, in contrast to the classical estuarine paradigm in which vertically sheared
576 baroclinic exchange flows provide the primary mechanism of dispersion. However, as Ri_e
577 becomes larger due either to an increase in river flow or decrease in tidal forcing, the system
578 transitions from lateral to vertical shear dominant. These results highlight how the dominant mode
579 of dispersion can vary for the same estuary geometry due to fortnightly and seasonal changes in
580 forcing.

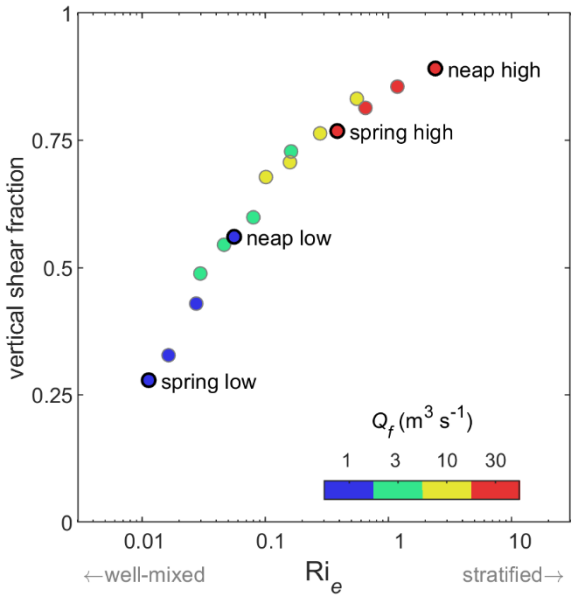

Figure 13. Relationship between the estuarine Richardson number and the fraction of the total dispersive salt flux due to vertical shear dispersion in the moving planes. Select model runs are labeled, with colors corresponding to the river discharge. Low values of the estuarine Richardson numbers are typically associated with well-mixed conditions whereas high values are more stratified.

5.5 *Dependence of tidal dispersion on estuarine lengthscales*

Finally, we note the increasing importance of tidal processes as the lengthscale of the estuarine salinity distribution, L_e, becomes shorter compared to the tidal excursion, L_t (Figure 14). We find that the relative contribution of nonlocal dispersion to the landward salt flux has a strong, consistent relationship to the lengthscale ratio, increasing from 20% for neap tides, low flow to 75% for spring tides, high flow (Figure 14a). The maximal nonlocal fraction occurs under the same conditions in which dispersion is dominated by processes outside the mouth, as observed previously in Figure 9c. This corresponds to the fact that shear dispersion outside the estuary can only contribute to the salt balance inside the estuary through the nonlocal salt flux.

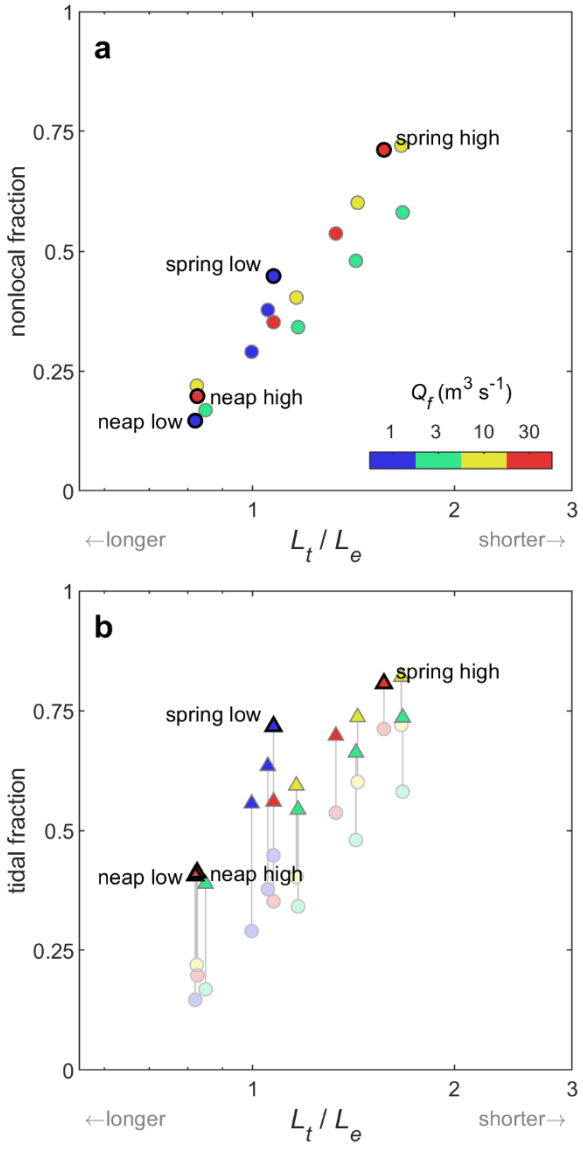

Figure 14. Ratio of the tidal excursion, L_t, to the estuary length, L_e, versus the (a) nonlocal and (b) tidal fraction of the total dispersive salt flux for each model run. Larger values of this ratio correspond to a shorter estuary. Select model runs are labeled, with colors corresponding to the river discharge. The tidal excursion is determined from the spatial extent of the 15-psu isohaline, while the estuary length is calculated from the tidal mean distance between the 2- and 28-psu isohalines. In (b), the triangles represent the total tidal dispersion fraction, the light circles represent the contribution of nonlocal salt flux to the tidal salt flux, and the length of each line corresponds to the remaining component of the tidal salt flux due to tidal component of the local dispersive salt flux.

We note that the nonlocal fraction accounts for only part of the tidal dispersion fraction, ν, as defined by Hansen and Rattray (1965), with the difference being the inclusion of the tidally varying component of the local dispersive salt flux in ν (Figure 14b). The contribution of the tidally varying component of the local dispersion only varies slightly with changes in forcing conditions, whereas the nonlocal contribution provides almost all of the variation of ν with respect to tidal forcing and river flow. Therefore, short estuaries will likely have a high value of ν primarily due to the increasing importance of nonlocal dispersion.

6 Conclusions

For short, tidally dominated estuaries, a significant fraction of the total dispersive salt flux results from nonlocal dispersion, that is, the oscillatory salt flux due to the correlation between the cross-sectionally averaged velocity and salinity. In this paper, we analyzed the nonlocal salt flux using the quasi-Lagrangian moving plane framework described by Dronkers and van de Kreeke (1986), which we have applied in practice for the first time. Our analyses revealed that in a plane moving with the tides along the channel of the estuary, all landward salt flux results from shear dispersion, i.e., spatial correlations of velocity and salinity over the cross-section. This analysis thus directly links the subtidal salt balance to the spatiotemporal variability of shear dispersion within the estuary and adjacent coastal waters near the mouth.

Hotspots of dispersion occur in space and time primarily due to instances of flow separation and tidal straining. The dispersive salt flux varies with the tidal currents and tidally varying position of the salinity gradient zone of the estuary with respect to topographic features. The relative importance of different dispersive mechanisms to the total landward salt flux varies with forcing conditions – lateral processes are most important during low river flow and spring tide conditions, whereas vertical processes become most important for high flow and neap tide.

We have shown that the DvdK86 framework provides a useful approach for studying the salt balance in estuaries where topography and the salinity distribution vary at lengthscales smaller than or similar to the tidal excursion. While the moving plane concept can be readily invoked to explain the nonlocal salt flux in any particular estuarine study, the application of this method is primarily suited for numerical modeling studies due to its requirement for high spatial and temporal resolution of the local dispersive salt fluxes.

Nevertheless, the insights gained from this study can be used to inform the investigation of salt fluxes in observational studies. Due to the spatiotemporal variability of the instantaneous local dispersive salt flux, careful placement of instruments as well as selection of sampling regions and periods must be considered. Similarly, the occurrence of dispersion hotspots suggests that only key regions of interest at select periods of the tidal cycle would need to be surveyed with high-resolution measurements to identify the most significant sources of the dispersive salt flux throughout the estuary. Thus, field efforts aimed at understanding salt fluxes in short estuaries should focus primarily on resolving the velocity and salinity structure when and where dispersion is locally enhanced, such as near topographic features like the mouth.

Data availability statement

The model output data used for analysis in the study are available at Woods Hole Open Access Server (WHOAS) via https://doi.org/10.26025/1912/28663.

Acknowledgements

This project was funded by NSF Grant OCE-1634490. The research presented here is also based upon work supported by the NSF Graduate Research Fellowship under Grant No. #1122374. The authors thank Tong Bo & David Ralston for helpful comments and discussion.

References

Banas, N. S., Hickey, B. M., MacCready, P., & Newton, J. A. (2004). Dynamics of Willapa Bay, Washington: A highly unsteady, partially mixed estuary. *Journal of Physical Oceanography*, *34*(11), 2413–2427. https://doi.org/10.1175/JPO2637.1

Blanckaert, K. (2010). Topographic steering, flow recirculation, velocity redistribution, and bed topography in sharp meander bends. *Water Resources Research*, *46*(9), 1–23. https://doi.org/10.1029/2009WR008303

Bo, T., & Ralston, D. K. (2020). Flow Separation and Increased Drag Coefficient in Estuarine Channels With Curvature. *Journal of Geophysical Research: Oceans*, *125*(10), 1–25. https://doi.org/10.1029/2020jc016267

Bowden, K. F. (1965). Horizontal mixing in the sea due to a shearing current. *Journal of Fluid Mechanics*, *21*, 83–95. https://doi.org/10.1007/BF00167972

Bowen, M. M., & Geyer, W. R. (2003). Salt transport and the time-dependent salt balance of a partially stratified estuary. *Journal of Geophysical Research*, *108*(C5), 3158. https://doi.org/10.1029/2001JC001231

Burchard, H., & Hetland, R. D. (2010). Quantifying the contributions of tidal straining and gravitational circulation to residual circulation in periodically stratified tidal estuaries. *Journal of Physical Oceanography*, *40*(6), 1243–1262. https://doi.org/10.1175/2010JPO4270.1

Chatwin, P. C. (1976). Some remarks on the maintenance of the salinity distribution in estuaries. *Estuarine and Coastal Marine Science*, *4*(5), 555–566. https://doi.org/10.1016/0302-3524(76)90030-X

Chen, S.-N., Geyer, W. R., Ralston, D. K., & Lerczak, J. A. (2012). Estuarine Exchange Flow

659 Quantified with Isohaline Coordinates: Contrasting Long and Short Estuaries. *Journal of*
660 *Physical Oceanography, 42*(5), 748–763. https://doi.org/10.1175/JPO-D-11-086.1
661 Dronkers, J. (1978). Longitudinal Dispersion in Shallow Well-Mixed Estuaries. In *Coastal*
662 *Engineering 1978* (Vol. 73, pp. 2761–2777). New York, NY: American Society of Civil
663 Engineers. https://doi.org/10.1061/9780872621909.171
664 Dronkers, J., & van de Kreeke, J. (1986). Experimental determination of salt intrusion mechanisms
665 in the Volkerak estuary. *Netherlands Journal of Sea Research, 20*(1), 1–19.
666 https://doi.org/10.1016/0077-7579(86)90056-6
667 Elder, J. W. (1959). The dispersion of marked fluid in turbulent shear flow. *Journal of Fluid*
668 *Mechanics, 5*(04), 544. https://doi.org/10.1017/S0022112059000374
669 Finotello, A., D'Alpaos, A., Bogoni, M., Ghinassi, M., & Lanzoni, S. (2020). Remotely-sensed
670 planform morphologies reveal fluvial and tidal nature of meandering channels. *Scientific*
671 *Reports, 10*(1), 1–13. https://doi.org/10.1038/s41598-019-56992-w
672 Fischer, H. B. (1972). Mass transport mechanisms in partially stratified estuaries. *Journal of Fluid*
673 *Mechanics, 53*(4), 671–687. https://doi.org/10.1017/S0022112072000412
674 Fischer, H. B., List, E. J., Koh, R. C. Y., Imberger, J., & Brooks, N. H. (1979). *Mixing in Inland*
675 *and Coastal Waters*. San Diego, California: Academic Press.
676 Fram, J. P., Martin, M. A., & Stacey, M. T. (2007). Dispersive fluxes between the coastal ocean
677 and a semienclosed estuarine basin. *Journal of Physical Oceanography, 37*(6), 1645–1660.
678 https://doi.org/10.1175/JPO3078.1
679 Garcia, A. M. P., Geyer, W. R., & Randall, N. (2021). Exchange Flows in Tributary Creeks
680 Enhance Dispersion by Tidal Trapping. *Estuaries and Coasts*.
681 https://doi.org/10.1007/s12237-021-00969-4

Geyer, W. R., & Signell, R. P. (1992). A Reassessment of the Role of Tidal Dispersion in Estuaries and Bays. *Estuaries*, *15*(2), 97. https://doi.org/10.2307/1352684

Geyer, W. R., Chant, R., & Houghton, R. (2008). Tidal and spring-neap variations in horizontal dispersion in a partially mixed estuary. *Journal of Geophysical Research: Oceans*, *113*(7), 1–16. https://doi.org/10.1029/2007JC004644

Grant, W. D., & Madsen, O. S. (1982). Movable bed roughness in unsteady oscillatory flow. *Journal of Geophysical Research*, *87*(C1), 469–481. https://doi.org/10.1029/JC087iC01p00469

Haidvogel, D. B., Arango, H., Budgell, W. P., Cornuelle, B. D., Curchitser, E., Di Lorenzo, E., et al. (2008). Ocean forecasting in terrain-following coordinates: Formulation and skill assessment of the Regional Ocean Modeling System. *Journal of Computational Physics*, *227*(7), 3595–3624. https://doi.org/10.1016/j.jcp.2007.06.016

Hansen, D. V., & Rattray, M. (1965). Gravitational circulation in straits and estuaries. *Journal of Marine Research*, *23*, 104–122. https://doi.org/10.1098/rspb.2009.2214

Hughes, F. W., & Rattray, M. (1980). Salt flux and mixing in the Columbia River Estuary. *Estuarine and Coastal Marine Science*, *10*(5), 479–493. https://doi.org/10.1016/S0302-3524(80)80070-3

Hunkins, K. (1981). Salt Dispersion in the Hudson Estuary. *Journal of Physical Oceanography*, *11*(5), 729–738. https://doi.org/10.1175/1520-0485(1981)011<0729:SDITHE>2.0.CO;2

Kantha, L. H., & Clayson, C. A. (1994). An improved mixed layer model for geophysical applications. *Journal of Geophysical Research*, *99*(C12), 25235. https://doi.org/10.1029/94JC02257

Kranenburg, W. M., Geyer, W. R., Garcia, A. M. P., & Ralston, D. K. (2019). Reversed Lateral

Circulation in a Sharp Estuarine Bend with Weak Stratification. *Journal of Physical Oceanography*, *49*(6), 1619–1637. https://doi.org/10.1175/JPO-D-18-0175.1

Langbein, W. B., & Leopold, L. B. (1970). River Meanders and the Theory of Minimum Variance. *Rivers and River Terraces*, 238–263. https://doi.org/10.1007/978-1-349-15382-4_9

Lerczak, J. A., Geyer, W. R., & Chant, R. J. (2006). Mechanisms Driving the Time-Dependent Salt Flux in a Partially Stratified Estuary. *Journal of Physical Oceanography*, *36*(12), 2296–2311. https://doi.org/10.1175/JPO2959.1

MacCready, P., & Geyer, W. R. (2010). Advances in Estuarine Physics. *Annual Review of Marine Science*, *2*(1), 35–58. https://doi.org/10.1146/annurev-marine-120308-081015

Okubo, A. (1973). Effect of shoreline irregularities on streamwise dispersion in estuaries and other embayments. *Netherlands Journal of Sea Research*, *6*(1–2), 213–224. https://doi.org/10.1016/0077-7579(73)90014-8

Ralston, D. K., & Stacey, M. T. (2005). Longitudinal dispersion and lateral circulation in the intertidal zone. *Journal of Geophysical Research C: Oceans*, *110*(7), 1–17. https://doi.org/10.1029/2005JC002888

Rozovskii, I. L. (1957). Flow of water in bends of open channels. *Academy of Sciences of Ukrainian S.S.R., Translated from Russian, Israel Program for Science Translation*.

Shchepetkin, A. F., & McWilliams, J. C. (2005). The regional oceanic modeling system (ROMS): A split-explicit, free-surface, topography-following-coordinate oceanic model. *Ocean Modelling*, *9*(4), 347–404. https://doi.org/10.1016/j.ocemod.2004.08.002

Simpson, J. H., Brown, J., Matthews, J., & Allen, G. (1990). Tidal Straining, Density Currents, and Stirring in the Control of Estuarine Stratification. *Estuaries*, *13*(2), 125. https://doi.org/10.2307/1351581

Simpson, J. H., Vennell, R., & Souza, A. J. (2001). The salt fluxes in a tidally-energetic estuary. *Estuarine, Coastal and Shelf Science*, *52*(1), 131–142. https://doi.org/10.1006/ecss.2000.0733

Stacey, M. T., Burau, J. R., & Monismith, S. G. (2001). Creation of residual flows in a partially stratified estuary. *Journal of Geophysical Research: Oceans*, *106*(C8), 17013–17037. https://doi.org/10.1029/2000JC000576

Stommel, H., & Farmer, H. G. (1952). *On the nature of estuarine circulation : part I (chapters 3 and 4)*. Woods Hole, MA: Woods Hole Oceanographic Institution. https://doi.org/10.1575/1912/2032

Taylor, G. I. (1953). Dispersion of Soluble Matter in Solvent Flowing Slowly through a Tube. *Proceedings of the Royal Society A: Mathematical, Physical and Engineering Sciences*, *219*(1137), 186–203. https://doi.org/10.1098/rspa.1953.0139

Taylor, G. I. (1954). The Dispersion of Matter in Turbulent Flow through a Pipe. *Proceedings of the Royal Society A: Mathematical, Physical and Engineering Sciences*, *223*(1155), 446–468. https://doi.org/10.1098/rspa.1954.0130

Umlauf, L., & Burchard, H. (2003). A generic length-scale equation for geophysical turbulence models. *Journal of Marine Research*, *61*(2), 235–265. https://doi.org/10.1357/002224003322005087

Uncles, R. J., Elliott, R. C. A., & Weston, S. A. (1985). Dispersion of salt and suspended sediment in a partly mixed estuary. *Estuaries*, *8*(3), 256–269. https://doi.org/10.2307/1351486

Warner, J. C., Sherwood, C. R., Arango, H. G., & Signell, R. P. (2005). Performance of four turbulence closure models implemented using a generic length scale method. *Ocean Modelling*, *8*(1–2), 81–113. https://doi.org/10.1016/j.ocemod.2003.12.003

751 Warner, J. C., Defne, Z., Haas, K., & Arango, H. G. (2013). A wetting and drying scheme for
752 ROMS. *Computers and Geosciences*, *58*, 54–61. https://doi.org/10.1016/j.cageo.2013.05.004
753 West, J. R., Uncles, R. J., Stephens, J. A., & Shiono, K. (1990). Longitudinal dispersion processes
754 in the upper tamar estuary. *Estuaries*, *13*(2), 118–124. https://doi.org/10.2307/1351580
755 Wu, H., & Zhu, J. (2010). Advection scheme with 3rd high-order spatial interpolation at the middle
756 temporal level and its application to saltwater intrusion in the Changjiang Estuary. *Ocean*
757 *Modelling*, *33*(1–2), 33–51. https://doi.org/10.1016/j.ocemod.2009.12.001
758 Zimmerman, J. T. F. (1986). The tidal whirlpool: A review of horizontal dispersion by tidal and
759 residual currents. *Netherlands Journal of Sea Research*, *20*(2–3), 133–154.
760 https://doi.org/10.1016/0077-7579(86)90037-2
761